JOURNAL OF AIRCRAFT
Vol. 30, No. 2, March–April 1993

Euler Study on Porous Transonic Airfoils with a View Toward Multipoint Design

Peter M. Hartwich*
ViGYAN, Inc., Hampton, Virginia 23666

Euler solutions for steady transonic flow ($0.63 \leq M_\infty \leq 0.8$, $0 \text{ deg} \leq \alpha \leq 2 \text{ deg}$) over NACA 0012 and supercritical airfoils with solid as well as porous surfaces suggest porosity as a means to realize multipoint design for transonic airfoils. The porous surfaces extend over at least 90% of the chord. The porosity distribution is described by a modified sine wave with several amplitudes. Either connected or separated cavities are assumed to lie underneath the upper and lower surfaces. Applied to a NACA 0012 airfoil, porosity generally increases lift, in some instances by up to 65%. Porous NACA 0012 airfoils in supercritical flow yield reductions of an order of magnitude in wave drag at constant lift, compared to their solid counterpart. Making the surface of a supercritical airfoil permeable also leads to sizeable reductions in wave drag at constant lift for overspeed conditions. The discussion of the computed results addresses issues such as grid sensitivity and checks for systematic errors.

Introduction

POROSITY has long been employed to remedy unwanted phenomena in aerodynamics. To mind come perforated walls in the test section of transonic wind tunnels to reduce blockage effects. Maestrello[1] utilized a porous centerbody plug to eliminate the "screeching" of supersonic jet exhausts. Several feasibility studies[2–12] in the 1980s demonstrated that porous surface patches on transonic airfoils can delay the drag-rise associated with energy losses due to shocks and separated boundary layers. The principle of this drag-reducing technique, often labeled as "shock venting," is illustrated in Fig. 1.

The schematic in Fig. 1 illustrates the effect of porosity on some supercritical flow past a NACA 0012 airfoil. The flow accelerates along the upper surface to supersonic speeds. As the flow travels further along the airfoil it encounters an adverse pressure gradient due to decreasing curvature. Without shock venting the flow would get shocked down to subsonic speeds by a strong normal shock. Besides causing wave drag this terminating shock is often sufficiently strong to cause a separation of the boundary layer, thereby further increasing total drag. As sketched in Fig. 1, placing a porous strip with a cavity below at the position of the shock induces the formation of a recirculation bubble. This bubble acts like a hump which leads to an oblique compression wave (which can be isentropic) that decreases the strength of the terminating normal shock. It should be mentioned that building airfoils with humps in their upper skin for achieving the same effect was actually considered.[3]

Numerical studies on shock venting have almost exclusively concentrated on mimicking experiments.[7,9,11,12] Thus, the porous surface patches were mostly chosen to be very narrow with their effectiveness confined to a small bandwidth of free-stream Mach number and incidence. On rare occasions, numericists have looked at more unusual porosity distributions[4,7] which extended over a large portion of the airfoil. Corresponding surface pressure plots indicated that not only the intended wave drag reduction was achieved, but that the entire flowfield around the airfoil was changed. The airfoil looked as if it changed its effective shape on a large scale as reflected by some "equivalent" solid airfoil contours.[4] Oddly, it appears that such effects were accepted as some sort of "curiosa" and their ramifications, particularly for aerodynamic design, were never explored.

The present report is the result of a computational pilot study on the possibility of using large porous surface patches with cavities beneath to modulate flows over baseline airfoils in such a way that they become mission adaptive. In other words, the concept of porosity is numerically explored to determine whether it is a suitable means to achieve multipoint design for transonic airfoils. The computational approach allowed for a faster and less expensive assessment of influencing parameters such as profile geometry, arrangement of porous surface patches, and degree of porosity, compared to an experimental study. The investigation was carried out with an in-house developed Euler solver,[14,15] GAUSS2. This is a time-implicit upwind method for the nonconservative Euler equations using floating shock fitting for accurate representations of shocks. This method has proven to be fast, accurate, and, perhaps most important, unusually grid insensitive. The use of a Navier-Stokes solver or some interactive boundary-layer method, which would principally allow for an assessment of viscous effects such as separation and viscous drag, was rejected because of uncertainties in the proper calibration of turbulence models.[9,11,12]

After a brief review of the technical approach, results will be presented for sub- and supercritical flow past two baseline configurations: 1) a NACA 0012 airfoil; and 2) a wing section at the break station of NASA's EET-SCW3 (energy efficient transport-supercritical wing 3) wind-tunnel model (see Ref.

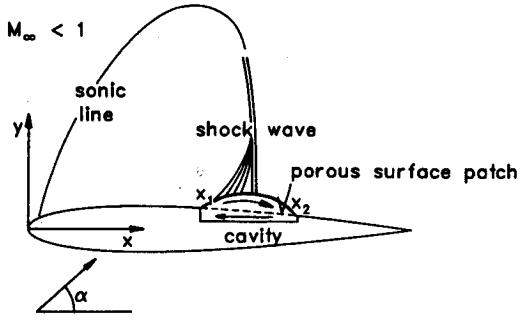

Fig. 1 Porous airfoil in transonic flow.

Received July 29, 1991; presented as Paper 91-3286 at the AIAA 9th Applied Aerodynamics Conference, Baltimore, MD, Sept. 23–25, 1991; revision received Dec. 30, 1991; accepted for publication Jan. 2, 1992.

*Research Scientist. Member AIAA.

16 and references cited therein). The effects of the degree of porosity, of connected/separated cavities beneath the upper and lower airfoil surfaces, and of the computational grid are assessed. Representative results indicate that the present approach is free of systematic errors, and that an alternate flow solver produces comparable results.

Technical Approach

Flow Solver

The two-dimensional, compressible, nonconservative Euler equations are solved on a structured body-fitted grid with a general time-implicit floating shock fitting method called GAUSS2. The details of the algorithm and code are presented elsewhere (see Refs. 14 and 15) and will only be briefly described here.

For reasons of computational speed, the upwinding is based on the nonconservative split coefficient method (SCM).[17] Nonconservative schemes can incorporate upwinding very cheaply, since the dependent variables can be chosen for convenience. Some "natural" choices are speed-of-sound and the Cartesian velocity components, because they are required in any upwind scheme. The set of dependent variables is completed by entropy which reduces the energy equation to a mere convection equation. All quantities are normalized with reference values for pressure, density, and length.

A floating shock fitting capability is implemented to achieve accuracy across shocks. Shocks are allowed to "freely" float between the grid points, and they are explicitly updated by way of the Rankine-Hugoniot relations. Away from shocks, fully one-sided, second-order accurate spatial differences are used. Differences across shocks are efficiently suppressed by way of operator arrays. The pertinent procedures contain several of Moretti's[18] ideas and notions with one crucial change: the shock orientation is computed locally by observing that the shock normal runs parallel to the change in velocity across shocks. The main advantage of the present approach to compute the shock orientation is that it eliminates the need to organize shock points in successive links. This improves computational efficiency (fewer "if" statements), avoids ill-defined shocks (e.g., so-called "isolated" shock points), and most importantly it forms a keystone for a straightforward extension of floating shock fitting to three dimensions.

The solution is implicitly advanced in time. Time accurate solutions for shocked flows, usually incommensurate with nonconservative methods, are computable by virtue of the shock-fitting technique. For time-accurate calculations the solutions are produced with second-order accurate Crank-Nicholson time differencing. For steady-state applications, a first-order accurate Euler-backward time discretization is preferred since it yields superior convergence performance due to its more suitable damping properties. Time dependency of the steady-state results is avoided by writing the discrete equations in delta form. The implicit operator is numerically inverted with a diagonalized approximate factorization (AF) algorithm.[19]

Computational Grids

The results for the solid and porous NACA 0012 airfoil were computed on a coarse and a standard C-type mesh. The standard mesh with 161 × 33 grid points has been closely patterned after that used in Refs. 14, 15, and 20 for computing subcritical shockless flow. The airfoil itself was covered with 133 grid points, and the spacing between the airfoil and the first points off the surface was on the order of 10^{-2} chords. A coarser grid was derived by dropping every other grid point in each coordinate direction. Although previous grid sensitivity studies[14,15] indicated that the standard grid is sufficient to resolve transonic inviscid flow past a NACA 0012 airfoil, some gridding effects were reassessed to rule out that the computed flowfield results are some grid-dependent artifacts.

The C-type grid around the EET-SCW3 wing section had, with 189 × 33 grid points, a slightly higher grid density than the grid around the NACA 0012 airfoils. The extra points were used for a sufficiently accurate surface definition of the more involved geometry of the supercritical airfoil. While retaining the same minimum spacing in radial direction around the airfoil as for the standard mesh around the NACA 0012 airfoil, the EET-SCW3 configuration was defined by 161 grid points.

For all grids the far field and the outflow boundaries were placed 6 chords away from the airfoils. Larger grid extents were without discernable effects on the computed flowfield results but required more computing time. The results were also unaffected by the grid type as indicated by control computations on O-type grids encompassing a NACA 0012 airfoil with 129 × 49 and 257 × 97 grid points.

Boundary and Initial Conditions

Since the subroutines setting the boundary conditions are modular elements which can be pulled out or plugged in as required by the subject flow problem, the boundary conditions are treated explicitly in time. Entropy along the airfoil is computed from simple extrapolation. The speed-of-sound along the profile is iteratively calculated from the momentum equations by simplifying η_x (ξ-momentum) + η_y (η-momentum)

$$-2\delta[U(\eta_x u_\xi + \eta_y v_\xi) + V(\eta_x u_\eta + \eta_y v_\eta)] = (\xi_x \eta_x + \xi_y \eta_y)(a^2)_\xi + (\eta_x^2 + \eta_y^2)(a^2)_\eta \quad (1)$$

where U and V are the contravariant velocity components

$$U = \xi_x u + \xi_y v \quad \text{and} \quad V = \eta_x u + \eta_y v \quad (2)$$

and $\delta = (\gamma - 1)/2$ with γ being the ratio of the specific heats. The velocity components along the airfoil are updated by evaluating

$$q_{\text{wall}} = q_{\text{wall}} + (v_n - V)n \quad (3)$$

where $q = (u, v)^T$ and $n = (\eta_x, \eta_y)^T$. The velocity components in q_{wall} are computed from linear extrapolation from the interior of the integration domain. For a solid airfoil surface, the transpiration velocity v_n is set to zero. Along a porous profile section v_n is evaluated by applying Darcy's law

$$v_n = -\sigma \frac{\Delta p}{\sqrt{\gamma} M_\infty} \quad (4)$$

where the subscript n indicates the direction of the outward facing surface normal. The proportionality factor σ is the porosity distribution function determined by viscosity as well as the permeability of the porous medium.[21] The expression Δp is defined by

$$\Delta p = p_{\text{wall}} - p_{\text{cavity}} \quad (5)$$

with

$$p_{\text{wall}} = (a_{\text{wall}}/\sqrt{\gamma})^{\gamma/\delta}/e^{\gamma s_{\text{wall}}}$$

As usually done,[4,7,9-12] the pressure in the cavity was assumed to be constant. Considering that the net mass flux through the porous surface of length L has to be zero for passive flow through the cavity, that is

$$\int_L \rho v_n \, ds = 0 \quad (6)$$

the cavity pressure can then be calculated as

$$p_{\text{cavity}} = \frac{\int_s \rho\sigma p_{\text{wall}}\, ds}{\int_s \rho\sigma\, ds} \tag{7}$$

The subsonic far-field boundary conditions along the perimeter of the integration domain are determined from characteristic-based formulations as readily found, e.g., in Ref. 22. Since these formulations adjust the freestream values for lifting effects, the circulation Γ of a potential vortex needs to be computed. Observing that $\Gamma \sim c_l$ (=sectional lift coefficient), and that provisions have to be made to deal with both solid as well as permeable airfoil surfaces; the airfoil lift coefficient for the scaling of the circulation is computed as

$$c_l = c_y \cos\alpha - c_x \sin\alpha \tag{8}$$

where c_x and c_y are the respective sectional force coefficients in x and y direction

$$c_x = \frac{2}{\gamma M_\infty^2}\left(\int_S p_{\text{wall}}\, dy - \int_S \rho_{\text{wall}} v_n u\, ds\right) \tag{9a}$$

$$c_y = \frac{-2}{\gamma M_\infty^2}\left(\int_S p_{\text{wall}}\, dx + \int_S \rho_{\text{wall}} v_n v\, ds\right) \tag{9b}$$

in which S is the circumference of the airfoil and u and v are the Cartesian velocity components along the profile.

The boundary conditions along the branch cut in the wake are updated by taking the average of the extrapolates from the interior of the integration domain, and the calculations were always started from freestream conditions.

Results

Solutions are shown for subcritical ($M_\infty = 0.63$, 0 deg $\leq \alpha \leq$ 2 deg) and supercritical ($M_\infty = 0.80$; 0 deg $\leq \alpha \leq$ 1.25 deg) flow over a solid ($\sigma_{\max} = 0$) and three porous ($\sigma_{\max} =$ 0.3, 0.6, and 0.9) NACA 0012 airfoils. In addition, results are presented for a solid and a porous ($\sigma_{\max} = 0.6$) EET-SCW3 wing section at test ($M_\infty = 0.71$, 0 deg $\leq \alpha \leq$ 1.25 deg) and overspeed ($M_\infty = 0.80$, 0 deg $\leq \alpha \leq$ 1.25 deg) conditions. The overspeed Mach number of 0.8 is equal to the test Mach number of the complete EET-SCW3 configuration. The equivalent test Mach number of 0.71 for the wing section at the break station of the EET-SCW3 configuration is derived from sweep theory. The porosity distribution is described by a "squared" sine wave[4,7]:

$$\sigma = \sigma_{\max}\sqrt{\sin\pi\frac{x - x_1}{x_2 - x_1}} \tag{10}$$

The subscripts 1 and 2 define the extent of the cavity (cf. Fig. 1). The values for x_1 and x_2 along both upper and lower surface of the NACA 0012 airfoil were 0 and 1, respectively, indicating that the porous surface patches extended of the entire chord. Since the supercritical EET-SCW3 wing section is characterized by a very thin trailing-edge region, the cavity is assumed to extend only over 90% of the chord, counting from the nose. Therefore, the corresponding values for x_1 and x_2 along the upper and lower surface are 0 and 0.9. The extent of the cavities was chosen to be as large as possible to achieve the maximum modulation effect on the surface pressure distribution. By virtue of the sinusoidal distribution function, porosity tapers off rapidly in the vicinity of the stagnation regions at the nose and trailing edge. Without this constraint the assumption of uniform pressure in the cavities would become questionable, and the flow in the cavity would actually have to be solved for. This issue was consciously avoided since an earlier attempt to account for the effects of an internal cavity flow yielded only inconclusive results,[12] and because such an effort would have been well beyond the scope of the present study.

The comparison of surface pressure distributions in Fig. 2 illustrates the effect of porosity on subcritical flow ($M_\infty =$ 0.63, $\alpha =$ 2 deg) past a NACA 0012 airfoil. The pressure distribution delineated by the solid line pertains to the solid NACA 0012 airfoil, and the symbols give the results for a profile with porous surfaces characterized by an intermediate value for $\sigma_{\max}$, which corresponds to a maximum geometric porosity (=hole area/surface area) of about 2.5%. The effects of higher or lower degrees of porosity (i.e., values for $\sigma_{\max}$) will be discussed below. The porous airfoil produces more than a 40% higher lift than its solid counterpart. This gain is primarily due to an inflection of the concave lee-side pressure distribution of the solid profile into a convex shape for the porous variant.

The variation of lift with angle of attack for subcritical flow ($M_\infty = 0.63$) over one solid ($\sigma_{\max} = 0$) and three porous ($\sigma_{\max} =$ 0.3, 0.6, and 0.9) NACA 0012 airfoils is plotted in Fig. 3. It appears that porosity emulates the effects of linearly varying camber as indicated by the steeper slopes of the curves for all porous variants of the NACA 0012 airfoil. Moreover, the gains in lift, which range from 20 to 65% based on the performance of the solid NACA 0012 profile, rise proportional to the degree of porosity. Intuitively, one expects this trend to approach some asymptotic limit which becomes apparent when supercritical flow past porous NACA 0012 airfoils is considered.

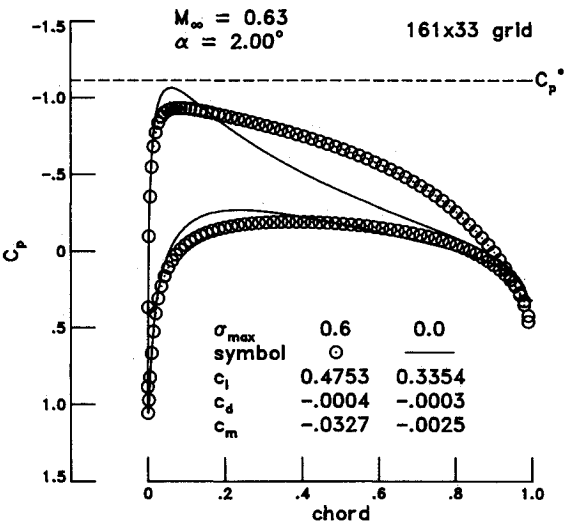

Fig. 2 Surface pressure distributions for porous and solid NACA 0012 airfoils in subcritical flow.

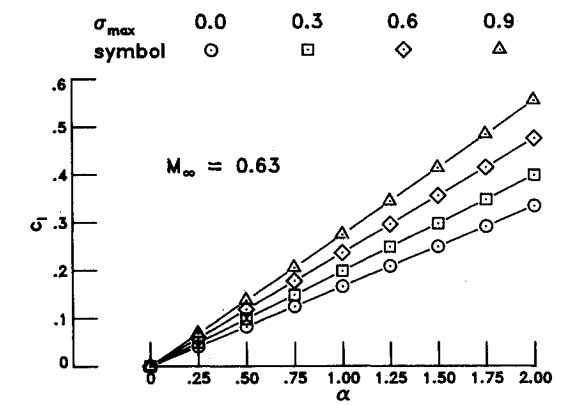

Fig. 3 Variation of lift with angle of attack for solid and porous NACA 0012 airfoils; subcritical flow.

The discussion of the results for supercritical flow past solid and porous NACA 0012 airfoils begins with an inspection of the effects of porosity on the surface pressure distribution for a particular flow case involving a permeable surface of intermediate porosity (i.e., $\sigma_{max} = 0.6$). Figure 4, which has the same layout as Fig. 2, shows a comparison between supercritical flow ($M_\infty = 0.8$, $\alpha = 1.25$ deg) over a porous ($\sigma_{max} = 0.6$) and a solid ($\sigma_{max} = 0$) NACA 0012 airfoil. A comparison of the force and moment coefficients reveals that the ratio of lift over wave drag for the porous airfoil is more than 2.5 times the value for the solid profile, and that this gain is achieved through increasing lift as well as by reducing wave drag. The gain in lift due to porosity is achieved through two mechanisms: 1) the pressure along the lower side is "equalized" and the supersonic regime, terminated by a weak shock, is eliminated; and 2) the supersonic regime along the upper surface of the profile is extended towards the trailing edge. The reduction in wave-drag stems from suppressing a supersonic regime along the lower airfoil surface, from having a lower shock Mach number, and from the formation of a λ shock above the airfoil.

The variation of lift with angle of attack for supercritical flow over one solid ($\sigma_{max} = 0$) and three porous ($\sigma_{max} = 0.3$, 0.6, and 0.9) NACA 0012 profiles is plotted in Fig. 5. The porous NACA 0012 airfoil with the lowest amplitude ($\sigma_{max} = 0.3$) in the porosity distribution produces only marginally more lift than its solid counterpart. The lift curves for the other two maximum values of porosity (i.e., $\sigma_{max} = 0.6$, and 0.9) lie close to each other and produce about the same amount of extra lift. Note that the bulk of the gain in lift stems from

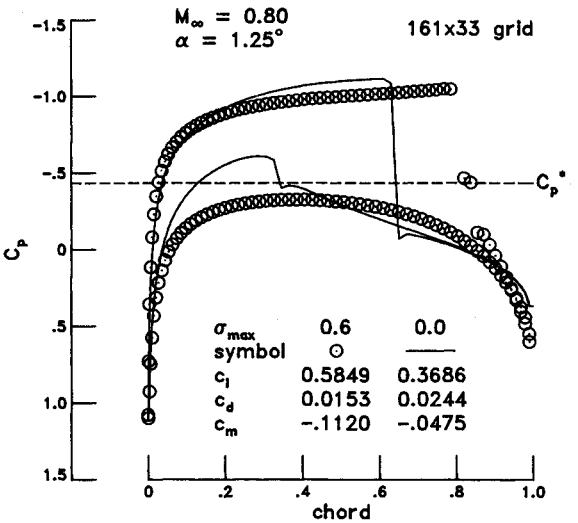

Fig. 4 Surface pressure distributions for porous and solid NACA 0012 airfoils in supercritical flow.

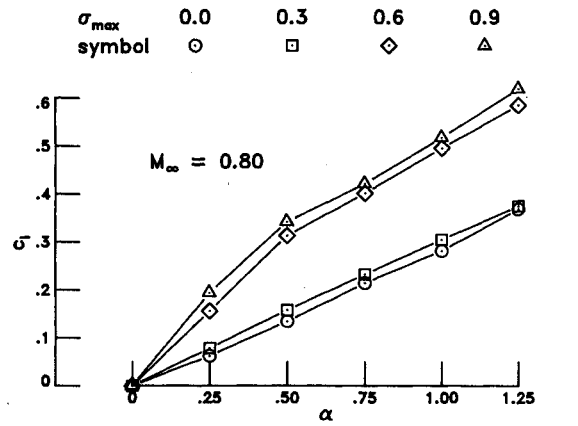

Fig. 5 Variation of lift with angle of attack for solid and porous NACA 0012 airfoils; supercritical flow.

the initially much steeper slope of the lift curves which both show a pronounced kink for $\alpha \approx 0.5$. For $\alpha > 0.5$, all curves have about the same slope, and the graphs for $\sigma_{max} = 0.6$ and 0.9 appear to be shifted from those for $\sigma_{max} = 0.0$ and 0.3, which reflects a camber effect.

The drag polars in Fig. 6 elucidate the behavior of the porous NACA 0012 airfoils in supercritical flow. The result points correspond to those in Fig. 3. Comparing the graphs for $\sigma_{max} = 0.0$ and 0.3 shows that for a given angle of attack the lowest degree of porosity leaves the lift almost unchanged while it significantly reduces the wave drag. For the two upper values of maximum porosity, a further reduction of wave drag (which when compared with the solid profile, can reach up to a full order of magnitude) is noticeable when the drag polars are compared for constant lift. When compared for constant angle of attack and with the constraint $\alpha \leq 0.5$ deg, it appears that the drag polars for $\sigma_{max} = 0.6$ and 0.9 are laterally shifted. That means that the airfoils with $\sigma_{max} \geq 0.6$ produce more lift for both incidence and wave drag being held constant. This is consistent with the initially steeper lift slope in Fig. 5, and it was confirmed by detailed comparisons of surface pressure distributions for several angles of attack and degrees of porosity. For $\alpha > 0.5$, the lift-enhancing qualities of porosity get overwhelmed by conventional angle-of-attack effects. The redistribution effects of porosity on the surface pressure along the upper airfoil surface fade out as the shock moves closer and closer to the trailing edge; the shock strength picks up and both lift, as well as wave drag, increase at about the same rate as for $\sigma_{max} \leq 0.3$. Finally, the results in Figs. 5 and 6 suggest that the effectiveness of porosity has indeed encountered a point of diminishing return for $\sigma_{max} \approx 0.6$ so that the discussion of the results in the remainder of this article will concentrate on comparing results for solid airfoils with porous profiles whose permeable surfaces are characterized by a value of $\sigma_{max} = 0.6$.

With the help of the DISC (direct iterative surface curvature) design tool,[23] equivalent airfoil shapes were computed using the porous pressure distributions in Figs. 2 and 4 as target pressures. The contours of these equivalent airfoil shapes are shown in a comparison with a NACA 0012 airfoil in Fig. 7. Both equivalent airfoils are characterized by a reduced nose radius and by a further aft position of their maximum thickness (about 45 vs 30% chord). Whereas the "supercritical" equivalent airfoil is only slightly thicker than the solid NACA 0012 profile and has just a small amount of camber, the "subcritical" equivalent airfoil is much thicker and shows a pronounced increase in camber. While the subcritical equivalent airfoil basically retains the basic shape of the NACA 0012 profile, the supercritical companion piece reveals a distinct flattening of the upper surface combined with a hump-shaped closure towards the trailing edge. Analyses of streamline patterns for the porous NACA 0012 profile at the corresponding flow conditions showed that the reduction in nose radius is

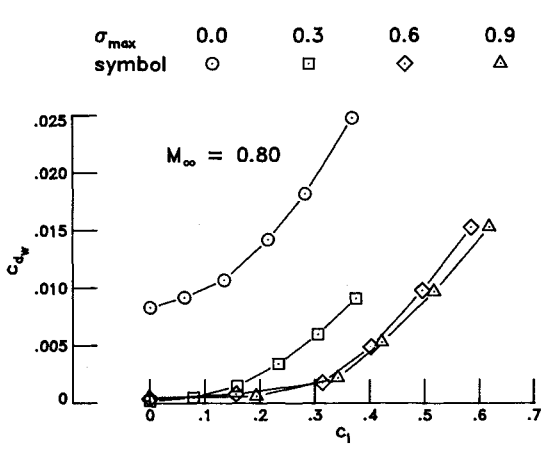

Fig. 6 Drag polars for solid and porous NACA 0012 airfoils.

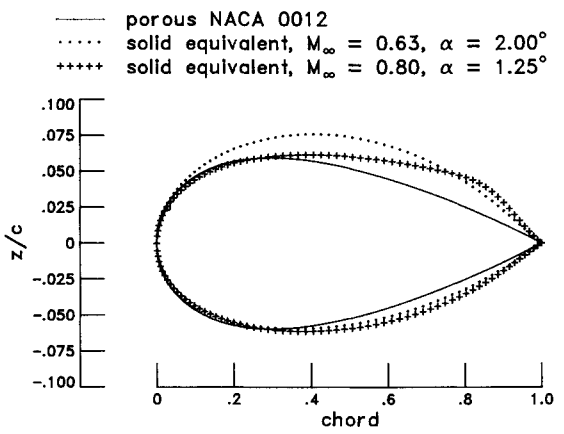

Fig. 7 Self-adaptive airfoil through porosity.

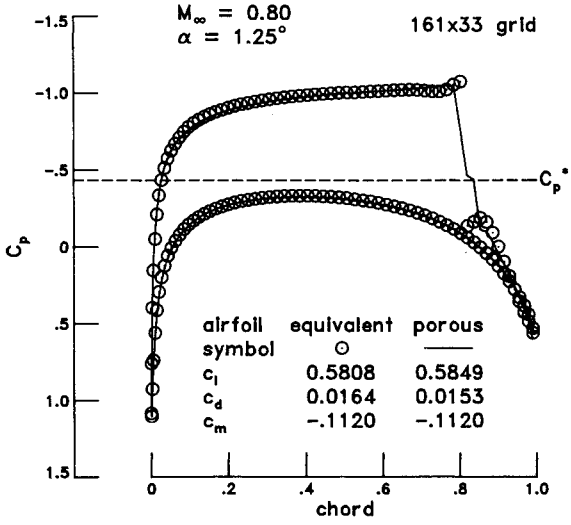

Fig. 8 Systematic error analysis using GAUSS2.

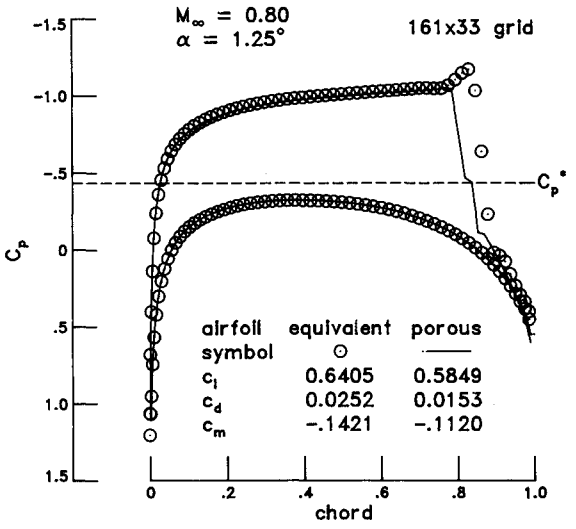

Fig. 9 Systematic error analysis using FLOMG.

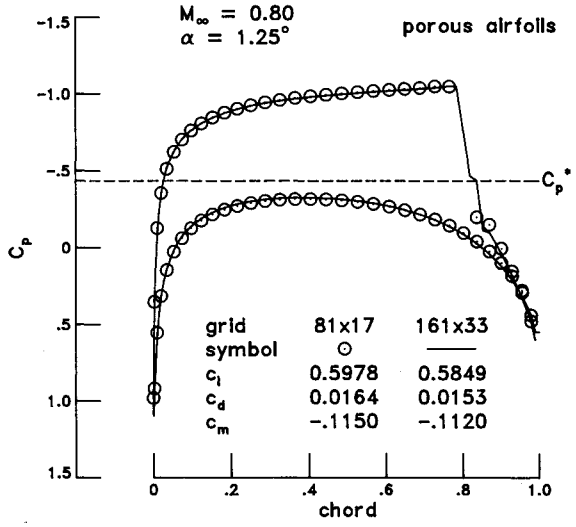

Fig. 10 Assessment of grid effect.

due to inflow into the cavities, and that the contours of the equivalent solid airfoils closely match the envelopes of recirculation bubbles.

As a check for systematic errors the flows over the equivalent solid airfoils in Fig. 7 were recomputed using the present shock fitting method GAUSS2, and an alternate shock capturing Euler solver, FLOMG.[24] Both codes produced very similar results for the subcritical flow case. The pertinent results with GAUSS2 and FLOMG for the supercritical flow case shown in Figs. 8 and 9. In these figures, the solid lines give the surface pressure distribution for the porous NACA 0012 airfoil as computed with GAUSS2 (compare with the symbols in Fig. 4). The symbols indicate the pressure distributions as computed with GAUSS2 (Fig. 8) and FLOMG (Fig. 9) for the solid, supercritical equivalent airfoil. Apart from expected minor differences in the vicinity of the shock, GAUSS2 gives very similar surface pressures for the porous NACA 0012 and the equivalent solid airfoil. That is also reflected by the closely matching values for the force and moment coefficients. Because the shock location in the FLOMG result is slightly further aft of those in the GAUSS2 predictions, FLOMG predicts higher values for the forces and moments. Nevertheless, the results with FLOMG support the trend of the GAUSS2 results.

As in previous analyses of solid transonic airfoils,[15] the floating shock fitting method was found to be unusually grid insensitive. This phenomenon is illustrated in Fig. 10 by comparison of the surface pressures for supercritical flow over a porous (σ_{max} = 0.6) NACA 0012 airfoil as computed on the standard grid of 161 × 33 grid points and on a coarser mesh with 81 × 17 nodes. Aside from the fact that the λ shock is resolved only on the standard mesh, both computations yield very similar surface pressure distributions, and predict within a bandwidth of about 2% the same lift and pitching moment. The larger margin of 7% between the predicted wave drag coefficients results mainly from the fact that the total loss of the two distinct shocks forming the legs of the λ shock is less than that of the single shock in the coarse grid calculation.

Figure 11 gives the convergence summaries for the flow cases discussed in Figs. 4 and 10. All calculations were run for 1000 cycles using local time stepping as a means to promote convergence towards a steady-state solution. While it appears that the solutions for the porous profile took a little longer to converge, the L_2 norm of all residuals was reduced by at least 5 orders of magnitude in all instances. The computing times are based on the flow solver's performance on NASA Langley's Cray-2s; the CPU time/node/cycle in single processor mode is about 6.5 μs. For completeness it is mentioned that the flow solver is written in standard FORTRAN 77 and requires about 65 words of memory per grid point.

Several flow cases were computed with the assumption of having upper and lower cavities connected in such a way that they form one cavity extending all the way from the trailing edge around the airfoil nose back to the trailing edge. The representative result in Fig. 12 indicates that while there is indeed very little wave drag, the lift has collapsed too. Even the ratio of lift to wave drag is lower than that of a porous NACA 0012 airfoil with separated cavities when compared for the same lift (see Fig. 6).

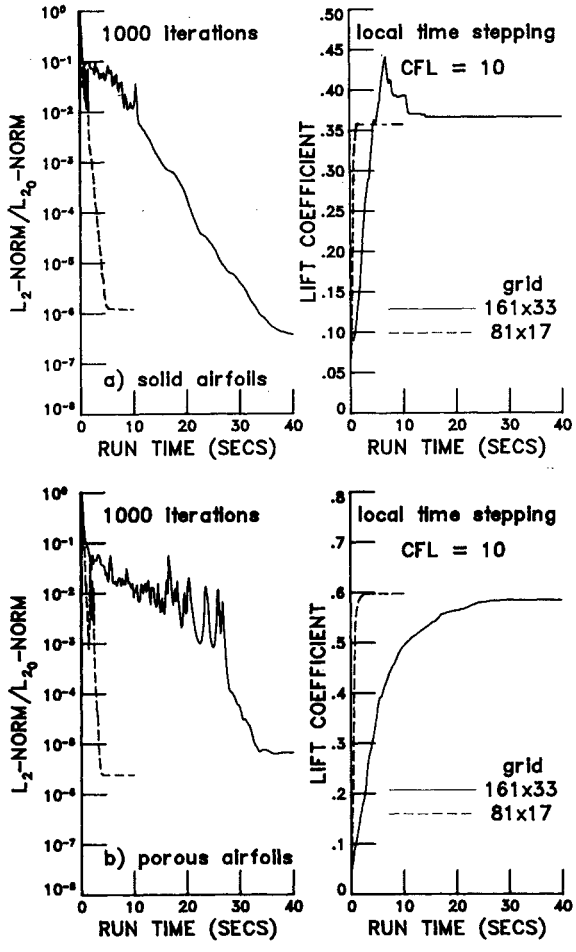

Fig. 11 Convergence summaries for supercritical flows past porous and solid NACA 0012 airfoils.

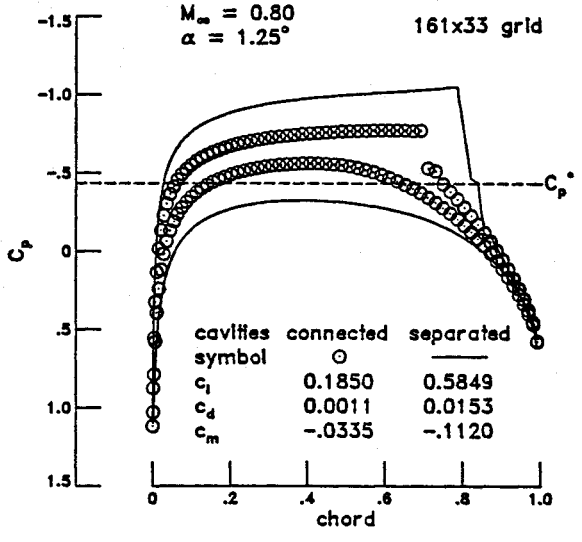

Fig. 12 Effect of connected vs separated cavities.

The results for the solid and porous NACA 0012 airfoils led to the question whether porosity might broaden the operational range for supercritical airfoils such as the EET-SCW3 wing section. The variation of lift with angle of attack in Fig. 13 shows mixed results. Four curves are plotted with porosity and Mach number as parameters. At the test Mach number of 0.71, the porous EET-SCW3 wing section produces less lift at low incidence but surpasses the lift of its solid counterpart at higher incidence by virtue of its steeper lift curve slope. At an overspeed condition (M_∞ = 0.8), the porous

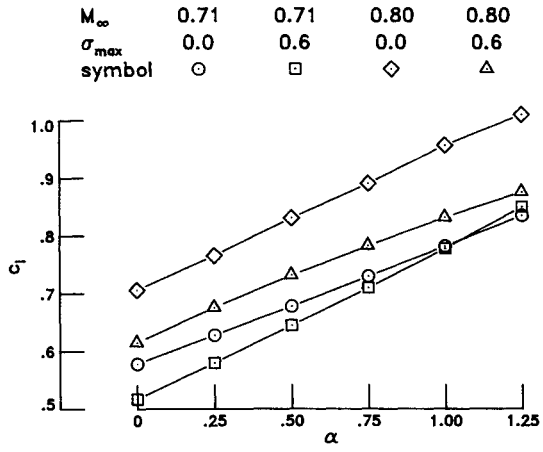

Fig. 13 Variation of lift with angle of attack for solid and porous EET-SCW3 wing sections.

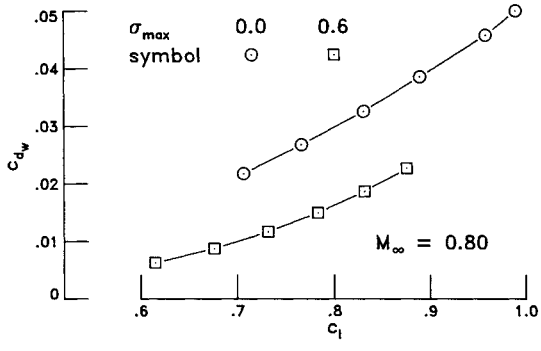

Fig. 14 Drag polars for solid and porous EET-SCW3 wing sections.

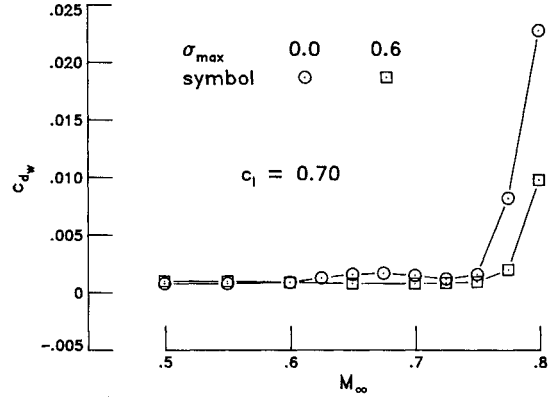

Fig. 15 Drag characteristics for solid and porous EET-SCW3 wing sections.

EET-SCW3 airfoil produces lower lift over the entire incidence range. Since the slopes of both lift curves for M_∞ = 0.8 are comparable, it looks like porosity "decambers" the supercritical airfoil.

The drag polars in Fig. 14 give a clearer picture for the effect of porosity on the performance of the EET-SCW3 wing section at overspeed conditions. While Fig. 14 again shows that porosity reduces lift at a given incidence, it also demonstrates that porosity also reduces wave drag. Comparing for the same lift, porosity improves wave drag by more than 100 counts.

The variation of wave drag with freestream Mach number for the design lift coefficient of c_l = 0.7 in Fig. 15 illustrates the potential of porosity for multipoint design for practical transonic airfoils. The solid supercritical airfoil develops a shock (albeit rather weak) in the nose region for $M_\infty \approx 0.625$. The strength of this shock reaches a maximum at $M_\infty \approx 0.675$. Since the angle of attack needs to be continuously reduced to maintain constant lift, the strength of this shock in the nose

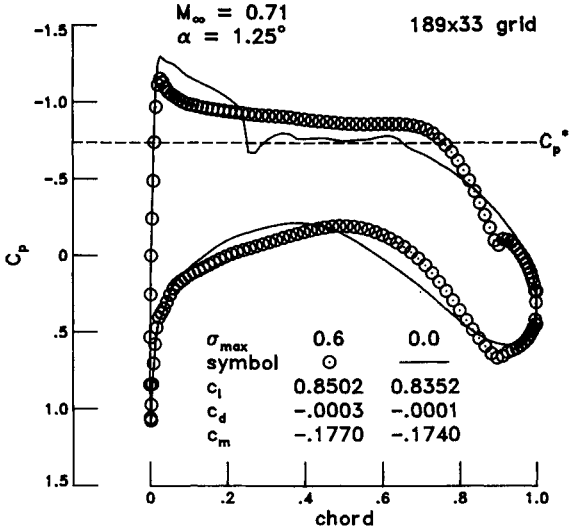

Fig. 16 Surface pressure distributions for solid and porous EET-SCW3 profiles at test conditions.

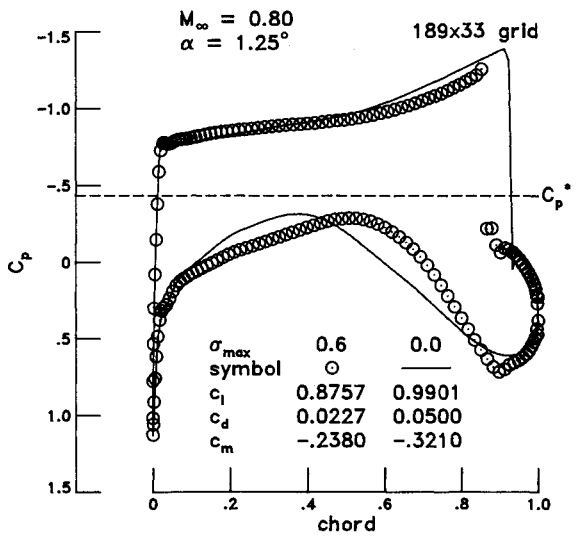

Fig. 17 Surface pressure distributions for solid and porous EET-SCW3 profiles at an overspeed condition.

region decreases until it reaches a minimum at $M_\infty \approx 0.75$. Beyond this point, the solid airfoil exhibits a sudden jump of the recompression shock into the aft part of the airfoil (i.e., $x/c > 0.7$) accompanied by an abrupt surge in wave drag. The porous version of the supercritical airfoil remains shock-free up to $M_\infty \approx 0.75$. Thus, porosity eliminates the drag creep at Mach numbers below design value and it also helps to undercut the wave drag of the solid supercritical airfoil at design conditions. Moreover, the porous supercritical airfoil delays drag rise by a margin of $\Delta M \approx 0.025$ by virtue of a softened onset of drag divergence compared to the more sudden jump associated with the solid supercritical profile.

Figures 16 and 17 illustrate the effects of porosity on the flow over the supercritical EET-SCW3 wing section at the test (Fig. 16) and the overspeed (Fig. 17) condition by comparing surface pressures for the solid airfoil and its porous counterpart. At the test condition porosity equalizes the surface pressure distribution without a major impact on the total area enveloped by the surface pressure contour. Therefore, the lift remains at roughly the same level. At the overspeed condition (Fig. 17), it looks like porosity fixes the location of the recompression shock, preventing it from moving further downstream and closer to the trailing edge. For the solid airfoil the shock is free to move aft, which yields additional lift at the expense of a significantly higher drag.

Conclusions

Euler analyses of transonic flow past NACA 0012 and supercritical airfoils indicated a potential of porosity for achieving a multipoint design for transonic airfoils. In particular, porous versions of the NACA 0012 airfoil demonstrated a new quality of being self-adaptive to dissimilar flow conditions. While a highly optimized supercritical airfoil was less impacted by porosity effects, it was demonstrated that porosity broadens its usable Mach number range. The next logical step is to verify these encouraging results in experimental proof-of-concept studies; the design and fabrication of suitable wind-tunnel models is currently underway.

Acknowledgments

NASA Langley Research Center sponsored this work under Contract NAS1-18585. L. Elwood Putnam suggested this research topic. His continued support and the contributions by Richard L. Campbell, James M. Luckring and Michael J. Hemsch in several fruitful discussions are gratefully acknowledged. Richard L. Campbell also provided the equivalent airfoil shapes using a design methodology developed by himself and Leigh Ann Smith; both also ran the computations with the alternate Euler solver on these equivalent airfoils.

References

[1]Maestrello, L., "An Experimental Study on Porous Plug Jet Noise Suppressor," AIAA Paper 79-0673, Seattle, WA, March 1979.

[2]Bahi, L., Ross, J. M., and Nagamatsu, H. T., "Passive Shock Wave/Boundary Layer Control for Transonic Airfoil Drag Reduction," AIAA Paper 83-0137, Reno, NV, Jan. 1983.

[3]Nagamatsu, H. T., Orozco, R. D., and Ling, D. C., "Porosity Effect on Supercritical Airfoil Drag Reduction by Shock Wave/Boundary Layer Control," AIAA Paper 84-1682, Snowmass, CO, June 1984.

[4]Savu, G., and Trifu, O., "Porous Airfoils in Transonic Flow," *AIAA Journal*, Vol. 22, No. 7, 1984, pp. 989–991.

[5]Krogmann, P., Stanewsky, E., and Thiede, P., "Effects of Suction on Shock/Boundary-Layer Interaction and Shock-Induced Separation," *Journal of Aircraft*, Vol. 22, No. 1, 1985, pp. 37–42.

[6]Nagamatsu, H. T., Dyer, R., and Ficarra, R. V., "Supercritical Airfoil Drag Reduction by Passive Shock Wave/Boundary Layer Control in the Mach Number Range .75 to .90," AIAA Paper 85-0207, Reno, NV, Jan. 1985.

[7]Chen, C.-L., Chow, C.-Y., Holst, T. L., and Van Dalsem, W. R., "Numerical Simulation of Transonic Flow Over Porous Airfoils," AIAA Paper 85-5022, Colorado Springs, CO, Oct. 1985.

[8]Raghunathan, S., and Mabey, D. G., "Passive Shockwave Boundary Layer Control Experiments on a Circular Arc Model," AIAA Paper 86-0285, Reno, NV, Jan. 1986.

[9]Olling, C. R., and Dulikravich, G. S., "Porous Aerofoil Analysis Using Viscous-Inviscid Coupling at Transonic Speeds," *International Journal for Numerical Methods in Fluids*, Vol. 7, No. 2, 1987, pp. 103–129.

[10]Hsieh, S.-J., and Lee, L.-C., "Numerical Simulation of Transonic Porous Airfoil Flows," *5th International Symposium on Numerical Methods in Engineering*, Springer-Verlag, New York, 1989, pp. 601–608.

[11]Chokani, N. D., and Squire, L. C., "Passive Control of Shock/Boundary Layer Interactions: Numerical and Experimental Studies," *Symposium Transonicum III*, Springer-Verlag, New York, 1989, pp. 399–406.

[12]Chen, C.-L., Chow, C.-Y., Van Dalsem, W. R., and Holst, T. L., "Computation of Viscous Transonic Flow over Porous Airfoils," *Journal of Aircraft*, Vol. 26, No. 12, 1989, pp. 1067–1075.

[13]Tai, T. C., Huson, G. G., Hicks, R. M., and Gregorek, G. M., "Transonic Characteristics of a Humped Airfoil," *Journal of Aircraft*, Vol. 25, No. 8, 1988, pp. 673, 674.

[14]Hartwich, P. M., "Fresh Look at Floating Shock Fitting," *AIAA Journal*, Vol. 29, No. 7, 1991, pp. 1084–1091.

[15]Hartwich, P. M., "Split Coefficient Matrix (SCM) Method with Floating Shock Fitting for Transonic Airfoils," *Lecture Notes in Physics*, Vol. 371, Springer-Verlag, New York, 1990, pp. 394–399.

[16]Waggoner, E. G., "Computational Transonic Analysis for an Advanced Transport Configuration with Engine Nacelles," AIAA

Paper 83-1851, Danvers, MA, July 1983.
[17]Chakravarthy, S. R., Anderson, D. A., and Salas, M. D., "The Split-Coefficient Matrix Method for Hyperbolic Systems of Gasdynamic Equations," AIAA Paper 80-0268, Pasadena, CA, Jan. 1980.
[18]Moretti, G., "A Technique for Integrating Two-Dimensional Euler Equations," *Computer and Fluids*, Vol. 15, No. 1, 1987, pp. 59–75.
[19]Pulliam, T. H., and Chaussee, D. S., "A Diagonal Form of an Implicit Approximate-Factorization Algorithm," *Journal of Computational Physics*, Vol. 39, No. 2, 1981, pp. 347–363.
[20]Pulliam, T. H., Jespersen, D. C., and Childs, R. E., "An Enhanced Version of an Implicit Code for the Euler Equations," AIAA Paper 83-0344, Reno, NV, Jan. 1983.
[21]Bird, R. B., Warren, E. S., and Lightfoot, E. N., *Transport Phenomena*, Wiley, New York, 1960, p. 150.
[22]Pulliam, T. H., and Steger, J. L., "Recent Improvements in Efficiency, Accuracy, and Convergence for Implicit Approximate Factorization Algorithms," AIAA Paper 85-0360, Reno, NV, Jan. 1985.
[23]Smith, L. A., and Campbell, R. L., "A Method for the Design of Transonic Flexible Wings," NASA TP 3045, Dec. 1990.
[24]Maksymiuk, C. M., Swanson, R. C., and Pulliam, T. H., "A Comparison of Two Central Difference Schemes for Solving the Navier-Stokes Equations," NASA TM 102815, July 1990.